Histone methylation regulator PTIP is required to maintain normal and leukemic bone marrow niches

Prosun Das[a], Kylee J. Veazey[a], Hieu T. Van[a], Saakshi Kaushik[a], Kevin Lin[a,b], Yue Lu[a,b], Masaru Ishii[c], Junichi Kikuta[c], Kai Ge[d], Andre Nussenzweig[e], and Margarida A. Santos[a,b,1]

[a]Department of Epigenetics and Molecular Carcinogenesis, University of Texas MD Anderson Cancer Center, Houston, TX 77030; [b]Center for Cancer Epigenetics, University of Texas MD Anderson Cancer Center, Houston, TX 77030; [c]Department of Immunology and Cell Biology, Graduate School of Medicine and Frontier Biosciences, Osaka University, Osaka 565-0871, Japan; [d]Laboratory of Endocrinology and Receptor Biology, National Institute of Diabetes and Digestive and Kidney Diseases, National Institutes of Health, Bethesda, MD 20892; and [e]Laboratory of Genome Integrity, National Cancer Institute, National Institutes of Health, Bethesda, MD 20892

Edited by Dennis A. Carson, University of California, San Diego, La Jolla, CA, and approved September 11, 2018 (received for review April 9, 2018)

The bone is essential for locomotion, calcium storage, and harboring the hematopoietic stem cells (HSCs) that supply the body with mature blood cells throughout life. HSCs reside at the interface of the bone and bone marrow (BM), where active bone remodeling takes place. Although the cellular components of the BM niche have been characterized, little is known about its epigenetic regulation. Here we find that the histone methylation regulator PTIP (Pax interaction with transcription-activation domain protein-1) is required to maintain the integrity of the BM niche by promoting osteoclast differentiation. PTIP directly promotes chromatin changes required for the expression of *Pparγ* (peroxisome proliferator-activated receptor-γ), a transcription factor essential for osteoclastogenesis. PTIP deletion leads to a drastic reduction of HSCs in the BM and induces extramedullary hematopoiesis. Furthermore, exposure of acute myeloid leukemia cells to a PTIP-deficient BM microenvironment leads to a reduction in leukemia-initiating cells and increased survival upon transplantation. Taken together, our data identify PTIP as an epigenetic regulator of osteoclastogenesis that is required for the integrity of the BM niche to sustain both normal hematopoiesis and leukemia.

epigenetics | osteoclasts | hematopoiesis | leukemia

The bone is a dynamic tissue that undergoes continual and tightly regulated remodeling, providing essential functions such as locomotive activity, storage of calcium, and the physical place where hematopoietic stem cells (HSCs) reside. The function of hosting HSCs is rather important, as these cells have the remarkable capacity to self-renew and differentiate to supply our body with more than 100 billion mature blood cells every day throughout life (1). HSCs reside in local tissue microenvironments that maintain and regulate their functions. In adulthood and under normal conditions, HSCs are found in the bone marrow (BM) within specialized niches.

The interface of bone and BM is known as the "endosteum," which is covered by bone-forming osteoblasts and bone-resorbing osteoclasts. The association of the endosteum with hematopoietic progenitor activity has been acknowledged for decades (2). Osteoblasts are cells of mesenchymal origin that have been shown to influence hematopoietic stem and progenitor cells (HSPCs). However, osteoblasts are thought not to regulate HSC maintenance directly but rather to act through cross-talk with other cell types in the BM (3–5).

Osteoclasts are large, multinucleated cells that differentiate from myeloid precursors and have emerged as important components of the BM niche (3, 6–9). These cells are positive for tartrate-resistant acid phosphatase (TRAP) activity and resorb bone tissue by secreting acids and endogenous collagenases. Ablation of osteoclasts in *oc*/*oc* mice leads to osteopetrosis and results in a dysfunctional HSC niche (8). It has also been shown that bone resorption and the subsequent release of calcium by osteoclasts promote HSC maintenance and localization to the endosteal region (6, 7).

The importance of understanding the cellular components of the HSC niche in detail is heightened by its involvement in hematological malignancies, particularly in myeloid neoplasms (10–15). Alterations in the BM niche are frequently observed in these cancers and contribute to the aggressive properties of leukemic-initiating cells (LICs). Increasing interest has been paid to targeting niche factors that draw LICs and their progeny out of the protected microenvironment and enhance their killing (16). Targeting the malignant BM microenvironment is appealing for several reasons: It could be (*i*) applied to various types of malignancies with different driver mutations, (*ii*) aimed to extinguish LICs at the expense of HSCs, thus avoiding remission, and (*iii*) used in combination with targeted therapies.

In recent years, several discoveries have identified niche components that can be manipulated to target self-reinforced malignant BM niches (12). Among myeloid malignancies, acute myeloid leukemias (AMLs) that harbor 11q23 translocations are associated with extremely poor prognosis and response to conventional therapies. Although a significant number of patients with refractory or relapsed disease will achieve remission,

Significance

Osteoclasts play an essential role in bone homeostasis. Understanding how osteoclast differentiation is regulated is important in the context of pathological bone conditions and the hematopoietic stem cell (HSC) niche. We show that PTIP directly promotes chromatin changes required for *Pparγ* expression, a transcription factor essential for osteoclastogenesis. Deletion of PTIP disrupts the integrity of the bone marrow (BM) niche, leading to a reduction of HSCs in the BM. Furthermore, a PTIP-deficient BM microenvironment decreases the number of acute myeloid leukemia-initiating cells in the BM and increases survival upon transplantation. Taken together, our data identify PTIP as an epigenetic regulator of osteoclastogenesis that is required for the integrity of the BM niche to sustain both normal hematopoiesis and leukemia.

Author contributions: P.D., M.I., J.K., K.G., A.N., and M.A.S. designed research; P.D., K.J.V., H.T.V., S.K., and J.K. performed research; K.G. and M.I. contributed new reagents/analytic tools; P.D., K.J.V., H.T.V., S.K., K.L., Y.L., M.I., J.K., and M.A.S. analyzed data; and P.D. and M.A.S. wrote the paper.

The authors declare no conflict of interest.

This article is a PNAS Direct Submission.

Data deposition: All raw and normalized RNA-sequencing data that support the findings of this study have been deposited in the Gene Expression Omnibus SuperSeries database (accession no. GSE118329).

[1]To whom correspondence should be addressed. Email: mialmeidasantos@mdanderson.org.

This article contains supporting information online at www.pnas.org/lookup/suppl/doi:10.1073/pnas.1806019115/-/DCSupplemental.

Published online October 8, 2018.

long-term survival rates remain poor, and new treatments are urgently needed (17). These leukemias harbor fusions of the *Mll1* (mixed lineage leukemia 1) gene to various partners that are members of protein complexes that affect transcriptional elongation (18–20). Leukemia-associated translocation breakpoints at *Mll1* and fusion partners are targeted by topoisomerase 2B at topological domain borders bound by CTCF (ccctc binding factor) and Cohesin (21). MLL-like complexes catalyze methylation of histone 3 at lysine 4 (H3K4me), which is associated with active gene expression (22). In addition to shared subunit composition, these complexes contain unique components which may provide target specificity to the complex. For example, PTIP (Pax interaction with transcription-activation domain protein-1) is a subunit of the MLL3 and MLL4 complex associated with gene activation (23–25). In addition to its role in transcription, PTIP is recruited to sites of DNA damage where it promotes double-strand break repair (26–28).

PTIP is essential for class-switch recombination in B lymphocytes (29), thymocyte development and migration (30), and humoral immunity (31); however, to our knowledge, a role for PTIP in sustaining BM hematopoiesis has not been reported. Here we show that PTIP deletion in HSPCs leads to extramedullary hematopoiesis accompanied by a disruption of the BM niche. Our studies reveal that PTIP is required for the integrity of the BM niche by promoting osteoclast differentiation. At the molecular level, we show that PTIP promotes chromatin changes required for the expression of *Pparγ* (peroxisome proliferator-activated receptor-γ), previously shown to be essential for osteoclastogenesis (32). Finally, we show that the effects of PTIP in the BM niche also extend to malignant hematopoiesis. Using a mouse model of *MLL*-rearranged AML, we show that exposure of leukemia cells to a PTIP-deficient BM microenvironment decreases the number of LICs and prolongs survival upon transplantation. Taken together, our data establish a role for PTIP in the regulation of osteoclastogenesis and the integrity of the BM niche, important for normal and leukemic stem cells.

Results

PTIP Deletion in HSCs and Progenitor Cells Leads to Extramedullary Hematopoiesis. Homozygous deletion of *Ptip* (also called "*Paxip1*") in mice results in lethality at E9.5 (33). To study the functions of PTIP in hematopoiesis, we crossed $Ptip^{flox/flox}$ mice (25) with IFN-inducible *Mx-1Cre* transgenic mice. To induce *Mx-1* expression and concomitant Cre-mediated recombination, we injected the animals in control and experimental groups with polyinosinic:polycytidylic acid [poly(I:C)] as previously described (34). Three weeks after the last poly(I:C) injection, we confirmed the deletion of PTIP by Western blot in hematopoietic-lineage cells from the BM of $Ptip^{flox/flox}$ *Mx-1Cre* mice compared with cells from WT *Mx-1Cre* mice also injected with poly(I:C) (herein called "$Ptip^{flox/flox}$ *Mx-1Cre*" mice and "WT *Mx-1Cre*" mice, respectively) (*SI Appendix*, Fig. S1*A*). Examination of $Ptip^{flox/flox}$ *Mx-1Cre* mice revealed splenomegaly and pale bones (Fig. 1*A* and *SI Appendix*, Fig. S1*B*). In addition, there was a pronounced accumulation of megakaryocytes in the spleen of $Ptip^{flox/flox}$ *Mx-1Cre* mice (Fig. 1*B*), indicative of extramedullary hematopoiesis. Quantification of live cells from BM and spleen showed that the cellularity was significantly decreased in the BM (Fig. 1*C*, *Left*) but was increased in the spleen (Fig. 1*C*, *Right*) of $Ptip^{flox/flox}$ *Mx-1Cre* mice. We observed a striking reduction in the numbers of Lin^{-} $cKit^{+}$ $Sca1^{+}$ (LSK) cells, a population that contains both the primitive HSCs and early progenitor cells, in the BM of $Ptip^{flox/flox}$ *Mx-1Cre* mice compared with controls (Fig. 1 *D* and *E*, *Left*). This was accompanied by a 10-fold increase of this population in the spleen (Fig. 1*E*, *Right*). Notably, WBC counts, RBC counts, and platelet counts (*SI Appendix*, Fig. S1*C*), as well as WBC differential counts (*SI Appendix*, Fig. S1*D*), were within the normal range in both WT *Mx-1Cre* and $Ptip^{flox/flox}$ *Mx-1Cre* mice, suggesting that HSPCs are capable of sustaining hematopoiesis in the absence of PTIP. To confirm this directly, we transplanted $CD45^{+}$ (cells of hematopoietic origin) BM cells from $Ptip^{flox/flox}$ *Mx-1Cre* animals before *cre* excision [no poly(I:C) injections] into lethally irradiated recipients. After 5 wk, half of the recipients were injected with poly(I:C) to delete PTIP in the hematopoietic cells, and the other half remained as controls (*SI Appendix*, Fig. S2*A*). As shown in *SI Appendix*, Fig. S2 *B* and *C*, both groups of recipients successfully reconstituted all blood lineages, independently of PTIP deletion. Taken together, our data show that HSPCs do not require PTIP to sustain hematopoiesis.

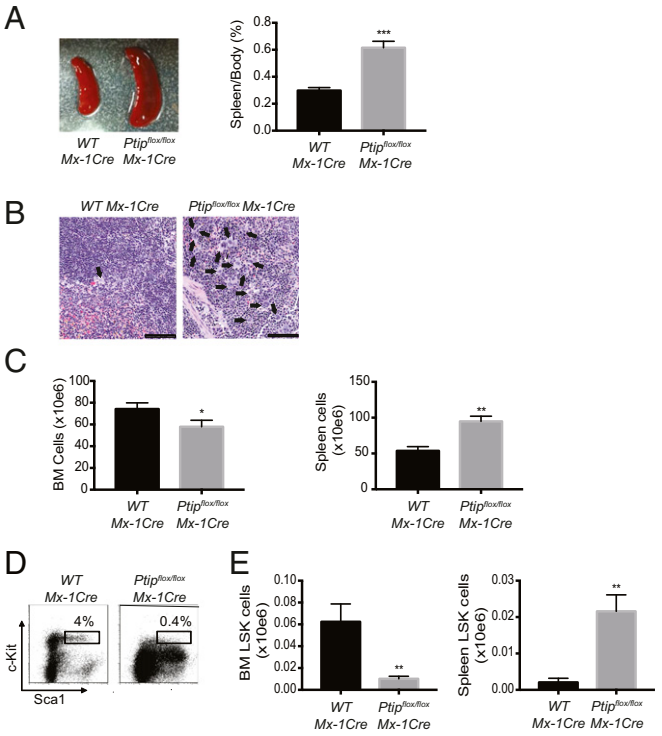

Fig. 1. PTIP deletion leads to extramedullary hematopoiesis in the spleen. (*A*) Gross morphology of spleens (*Left*) and spleen-to-body weight ratio (*Right*, $n = 5$) of experimental WT *Mx-1Cre* and $Ptip^{flox/flox}$ *Mx-1Cre* mice 3 wk after injection with poly(I:C). (*B*) Histology of spleens isolated in *A*. Black arrows indicate megakaryocytes. (Scale bars: 100 μm.) (*C*) Total number of cells in the BM (*Left*, $n = 6$) and in spleen (*Right*, $n = 5$). (*D*) Flow cytometry showing the percentage of BM HSPCs, defined as LSK cells. One representative of three experiments is shown. (*E*) Total number of LSK cells in the BM (*Left*) and in the spleen (*Right*); $n = 5$. Bar graphs show mean ± SEM. $^{*}P < 0.05$; $^{**}P < 0.01$; $^{***}P < 0.005$.

To further demonstrate that the reduction of HSPCs in the BM and the extramedullary hematopoiesis in PTIP-deficient animals are not due to cell-intrinsic effects of PTIP deletion in HSPCs, we performed BM chimeras in which poly(I:C)-treated $Ptip^{flox/flox}$ *Mx-1Cre* BM cells (CD45.2) were mixed with WT BM cells (CD45.1) in a 1:1 ratio and were injected into poly(I:C)-treated WT *Mx-1Cre* or $Ptip^{flox/flox}$ *Mx-1Cre* recipients (*SI Appendix*, Fig. S3*A*). Eleven weeks after transplantation, we observed that the $Ptip^{flox/flox}$ *Mx-1Cre* recipients showed a reduction in the number of total BM cells and an increase in the number of total spleen cells (*SI Appendix*, Fig. S3*B*, *Left* for BM and *Right* for spleen) compared with WT *Mx-1Cre* recipients. We also observed that the number of WT LSK cells was decreased in the BM and increased in the spleen of $Ptip^{flox/flox}$ *Mx-1Cre* recipients (*SI Appendix*, Fig. S3*C*, *Left* for BM and *Right* for spleen) compared with WT LSK cells in WT *Mx-1Cre* animals. These findings further support the proposal that the observed phenotypes in

Ptip$^{flox/flox}$ *Mx-1Cre* mice are due to an LSK extrinsic effect within the BM compartment.

Increased Bone Volume and Decreased Medullary Space in the Absence of PTIP. Adult hematopoiesis happens mainly in the BM, and recent progress has been made in elucidating the location and cellular components of the HSC niche in the BM that includes the osseous environment, commonly known as the "endosteal niche" (3). Thus, we next examined bone volume and mineral density using microcomputed tomography (μCT) imaging (Fig. 2 *A*–*D*). Images of the sagittal (*Upper*) and transaxial (*Lower*) regions of the femur (Fig. 2*A*) showed an increase in bone volume with a reduced medullary cavity space in *Ptip*$^{flox/flox}$ *Mx-1Cre* mice compared with control animals. Consistently with this, static bone histomorphometry showed increased bone volume fraction (Fig. 2*B*) and trabecular number (Fig. 2*C*), with a decreased trabecular separation (Fig. 2*D*). Whole-body X-ray analysis revealed increased radio density in the skull, vertebrae, and long bones (Fig. 2*E*). Histology analysis of H&E staining of femur trabecular (Fig. 2*F*, *Upper*) and cortical (Fig. 2*F*, *Lower*) regions also supported the osteopetrotic phenotype of *Ptip*$^{flox/flox}$ *Mx-1Cre* animals observed by μCT and X-ray imaging. Taken together, these data show that PTIP deletion in HSPCs leads to increased bone mass, reduced medullary cavity space, and altered bone remodeling.

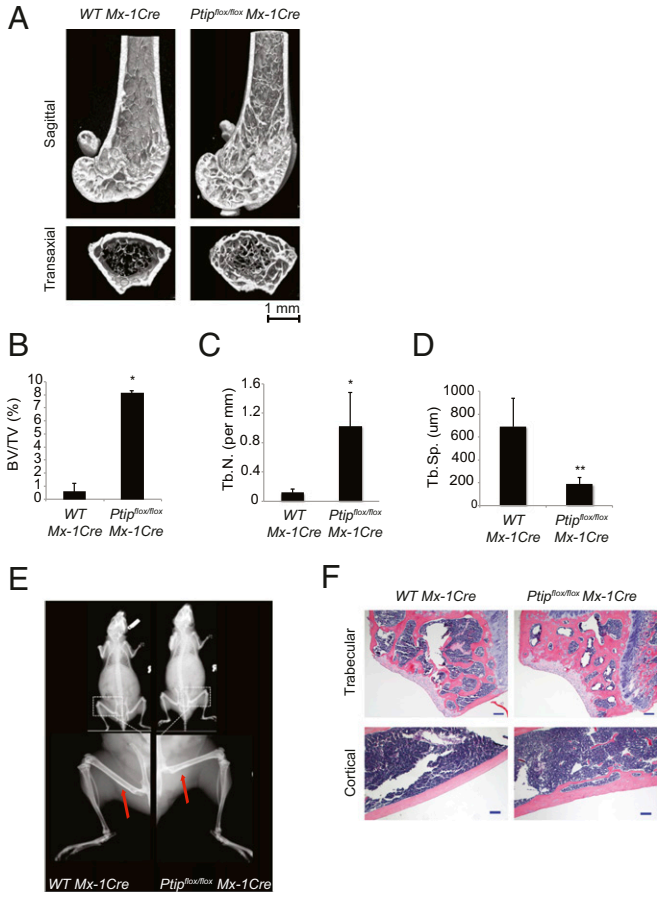

Fig. 2. PTIP deletion leads to increased bone volume and decreased medullary space. (*A*) μCT analysis of the sagittal (*Upper*) and transaxial (*Lower*) regions of femurs in WT *Mx-1Cre* and *Ptip*$^{flox/flox}$ *Mx-1Cre* mice 3 wk after poly(I:C) injection. (*B*–*D*) Static histomorphometric parameters, including bone volume (*B*), trabecular number (*C*), and trabecular separation (*D*) in WT *Mx-1Cre* and *Ptip*$^{flox/flox}$ *Mx-1Cre* littermates ($n = 3$) 3 wk after poly(I:C) injection. BV/TV (%), trabecular bone volume/total tissue volume in percentage; Tb.N, trabecular number per mm; Tb.Sp, trabecular separation in μm. (*E*) Whole-body X-ray analysis (*Upper*) and enlarged images (*Lower*) of long bones of WT *Mx-1Cre* and *Ptip*$^{flox/flox}$ *Mx-1Cre* mice 3 wk after poly(I:C) injection. Red arrows indicate the decreased size of the medullary cavity in the femur of *Ptip*$^{flox/flox}$ *Mx-1Cre* mice compared with control animals. (*F*) H&E-stained sections of the trabecular (*Upper*) and cortical (*Lower*) regions of femurs from WT *Mx-1Cre* and *Ptip*$^{flox/flox}$ *Mx-1Cre* mice 3 wk after poly(I:C) injection. (Scale bars: *Upper*, 100 mm; *Lower*, 200 mm.) Bar graphs show mean ± SEM. $^{*}P < 0.05$; $^{**}P < 0.01$.

PTIP Is Required for Osteoclast Differentiation. Bone is a composite tissue that undergoes a continual remodeling through the concerted and sequential effort of bone-forming osteoblasts and bone-resorbing osteoclasts (35). Osteoclasts derive from monocytes (hematopoietic lineage); osteoblasts derive from mesenchymal progenitors. Since the *Mx-1Cre* transgene allows the deletion of PTIP in cells of hematopoietic origin but not of mesenchymal origin, we hypothesized that the increase in bone volume and decreased medullary space observed in *Ptip*$^{flox/flox}$ *Mx-1Cre* mice (Fig. 2) could be a result of osteoclast defects. To test this directly, we performed alkaline phosphatase (ALP) staining of femur sections and observed that the number of ALP^{+} osteoblasts was unaffected by the deletion of PTIP (Fig. 3 *C* and *D*). In contrast, TRAP staining of femur sections revealed that the number of mature osteoclasts was lower in the mutant mice (Fig. 3 *A* and *B*). Furthermore, urine deoxypyridinoline levels were significantly lower in *Ptip*$^{flox/flox}$ *Mx-1Cre* mice (Fig. 3*E*), suggesting decreased bone resorption; in contrast, serum osteocalcin and ALP levels were normal, suggesting unaltered bone formation (Fig. 3 *F* and *G*). These results suggest that the osteopetrosis observed in *Ptip*$^{flox/flox}$ *Mx-1Cre* mice was mainly due to a decrease in osteoclast numbers and concomitant decrease in bone resorption.

Osteoclasts differentiate from monocytes under the influence of the cytokines macrophage colony-stimulating factor (M-CSF) and receptor activator of NF-κB ligand (RANKL) (36). We observed no significant differences in the numbers of monocyte progenitors (defined as Mac-1^{+} and Gr-1^{-} BM cells) (*SI Appendix*, Fig. S4*A*) or of osteoclast progenitors (defined as B220/CD3^{-}, Mac-1^{-}, and CD115^{+} BM cells) (*SI Appendix*, Fig. S4*B*) in PTIP-deficient BM compared with control. However, the number of mature osteoclasts (defined as RANK^{+} BM cells) was significantly reduced in PTIP-deficient BM compared with control BM (*SI Appendix*, Fig. S4*C*). These data suggest that PTIP deletion affects the differentiation of monocytes and osteoclast progenitors into differentiated osteoclasts.

Next, we directly assessed the effect of PTIP deletion on RANKL-induced osteoclast differentiation from spleen progenitor cells in an in vitro culture system widely used to study osteoclast differentiation (*SI Appendix*, Fig. S4*D*) (37). After RANKL treatment, the number of mature osteoclasts (represented by multinucleated TRAP^{+} cells) developed in WT cultures was significantly higher than the number of mature osteoclasts in the mutant cultures (Fig. 3 *H* and *I*). Because the number of HSPCs was higher in the spleens of *Ptip*$^{flox/flox}$ *Mx-1Cre* mice (Fig. 1*E*, *Right*), the decrease in osteoclast numbers was not due to a lack of progenitor cells but rather was due to intrinsic defects in RANKL-mediated osteoclast differentiation. This is also evidenced by the increased number of total cells recovered at the end of the cultures (day 7) (*SI Appendix*, Fig. S4*E*). We also performed this assay using BM cells and observed decreased osteoclast numbers in PTIP-deficient cells (*SI Appendix*, Fig. S5 *A* and *B*). Taken together, the results from both our ex vivo and in vitro experiments show that PTIP promotes osteoclast differentiation.

PTIP Promotes Osteoclast Differentiation by Transcriptional Regulation of *Pparγ*. Mature osteoclasts have a specific gene signature associated with extracellular matrix degradation and bone resorption

MEDICAL SCIENCES

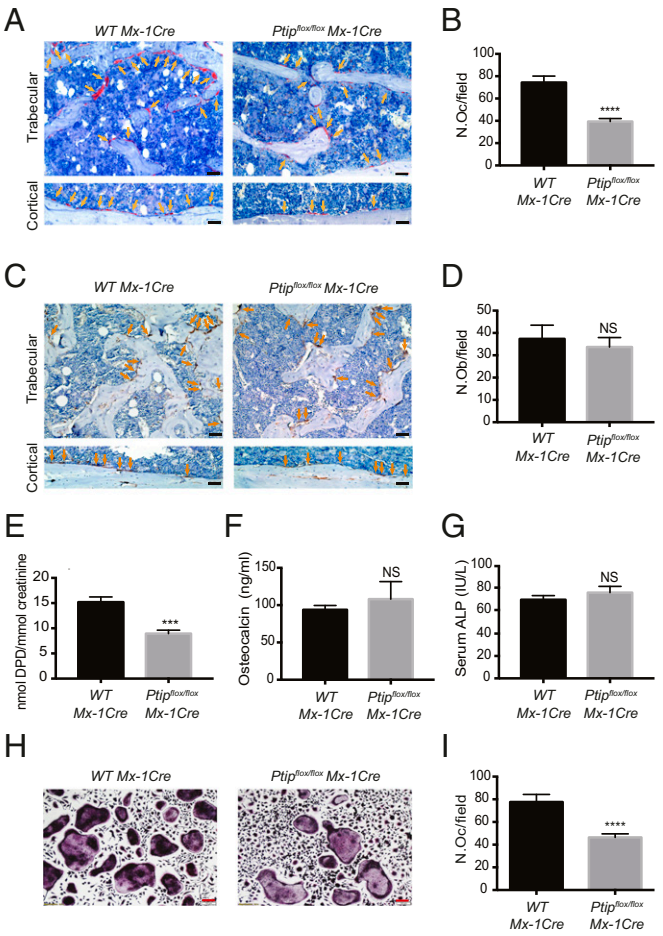

Fig. 3. PTIP is required for osteoclast differentiation. (*A*) TRAP staining of osteoclasts in femur sections of WT *Mx-1Cre* and *Ptip*$^{flox/flox}$ *Mx-1Cre* mice 3 wk after poly(I:C) injection. Orange arrows indicate osteoclasts. (Scale bars: 50 μm.) (*B*) Quantification of osteoclast cells in TRAP-stained tissue sections ($n = 4$). N.Oc/field, number of osteoclasts per field of view. (*C*) ALP staining of osteoblasts in femur sections of WT *Mx-1Cre* and *Ptip*$^{flox/flox}$ *Mx-1Cre* mice. Orange arrows indicate osteoblasts. (Scale bars: 50 μm.) (*D*) Quantification of osteoblast cells in ALP-stained tissue sections ($n = 4$). N.Ob/field, number of osteoblasts per field of view. (*E*) Detection of deoxypyridinoline (DPD) bone resorption marker in the urine of WT *Mx-1Cre* and *Ptip*$^{flox/flox}$ *Mx-1Cre* mice after poly(I:C) injection ($n = 6$). (*F*) Detection of osteocalcin bone-formation marker levels in blood serum of WT *Mx-1Cre* and *Ptip*$^{flox/flox}$ *Mx-1Cre* mice after poly(I:C) injection ($n = 8$). (*G*) Detection of ALP bone-formation marker levels in blood serum of WT *Mx-1Cre* and *Ptip*$^{flox/flox}$ *Mx-1Cre* mice after poly (I:C) injection ($n = 10$). (*H*) Representative pictures of mature multinucleated TRAP^{+} osteoclasts differentiated in vitro from splenocytes of WT *Mx-1Cre* and *Ptip*$^{flox/flox}$ *Mx-1Cre* mice after poly(I:C) injection. (Scale bars: 100 μm.) (*I*) Quantification of mature osteoclasts ($n = 3$). N.Oc/field, number of osteoclasts per field of view. Bar graphs show mean ± SEM. ***$P < 0.005$; ****$P < 0.0001$; NS, not significant ($P > 0.05$).

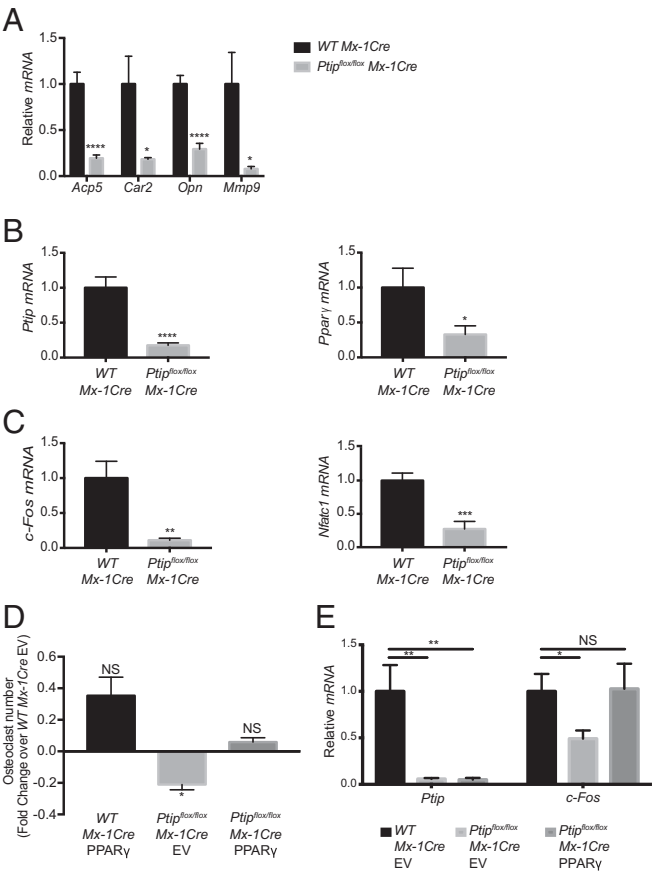

Fig. 4. PTIP regulates osteoclast differentiation by regulating *Pparγ* expression. (*A*–*C*) mRNA levels of osteoclast-specific genes: *Acp5* (TRAP), *Car2* (carbonic anhydrase-2), *Opn* (osteopontin), and *Mmp9* (matrix metallopeptidase-9) (*A*); *Ptip* (*B*, *Left*) and *Pparγ* (*B*, *Right*); and *c-Fos* (*C*, *Left*) and *Nfatc1* (*C*, *Right*) in splenocyte-derived osteoclast differentiation cultures 3 d after RANKL treatment ($n = 3$). (*D*) The effects of ectopic *Pparγ* expression on osteoclast differentiation were expressed as the fold change in the number of osteoclasts derived from splenocytes of WT *Mx-1Cre* and *Ptip*$^{flox/flox}$ *Mx-1Cre* mice infected with empty vector (EV) virus or *Pparγ* overexpression (Pparγ) virus compared with the number of osteoclasts derived from splenocytes of WT *Mx-1Cre* mice infected with empty vector ($n =$ 5–7, in three independent experiments). (*E*) *Ptip* and *c-Fos mRNA* levels in splenocyte-derived osteoclast-differentiation cultures infected with virus as in *D* 3 d after RANKL treatment ($n = 3$). Bar graphs show mean ± SEM. *$P <$ 0.05; **$P < 0.01$; ***$P < 0.005$; ****$P < 0.0001$; NS, not significant ($P > 0.05$).

(38). These genes encode proteins that include TRAP, carbonic anhydrase-2, osteopontin, and matrix metalloproteinase-9. We measured the expression of these genes in spleen and BM osteoclast-differentiation cultures (Fig. 4*A* and *SI Appendix*, Fig. S5*C*, respectively) and observed a significant reduction in the expression levels in the mutant cells compared with control cells. These results confirm that PTIP stimulates osteoclast differentiation at the transcriptional level.

Binding of the RANK receptor with its ligand RANKL triggers a signaling cascade controlling osteoclast lineage commitment and activation (37, 39). Pparγ has been shown to regulate this process in mice (32). Since PTIP was shown to directly regulate *Pparγ* during adipogenesis (40), we hypothesized that PTIP mediates osteoclast differentiation through transcriptional regulation of *Pparγ*. We measured *Pparγ* transcript levels in the RANKL-treated spleen- and BM-derived osteoclasts and found that the expression of *Pparγ* was reduced significantly, to an extent similar to that of *PTIP* expression, in cells obtained from *Ptip*$^{flox/flox}$ *Mx-1Cre* mice compared with cells from WT *Mx-1Cre* mice (Fig. 4*B* and *SI Appendix*, Fig. S5*D*, respectively). RANKL induces the expression of the *c-Fos osteosarcoma oncogene* (*c-Fos*), an important mediator of osteoclastogenesis, as mice lacking c-Fos develop osteopetrosis due to a block in osteoclast differentiation (41). *Pparγ* directs osteoclast differentiation through direct regulation of *c-Fos* (32). Consistently with a decrease in *Pparγ* levels, we also observed a significant decrease in *c-Fos* and its downstream osteoclast differentiation transcription regulator, *nuclear factor of activated T-cells, cytoplasmic, calcineurin-dependent 1* (*Nfatc1*) in PTIP-deficient cells compared with controls (Fig. 4*C* and *SI Appendix*, Fig. S5*E*).

We next evaluated whether ectopic expression of *Pparγ* could rescue the osteoclast differentiation blockade observed in the absence of PTIP. We used retrovirus-mediated gene transfer and confirmed *Pparγ* overexpression levels by RT-qPCR (*SI Appendix*, Fig. S6*A*). The number of osteoclasts differentiated from *Ptip*$^{flox/flox}$ *Mx-1Cre* splenocytes infected with *Pparγ* virus was increased by about 30% compared with *Ptip*$^{flox/flox}$ *Mx-1Cre* splenocytes infected with the empty vector virus (Fig. 4*D*). Thus, ectopic expression of *Pparγ* restores the number of osteoclasts differentiating from *Ptip*$^{flox/flox}$ *Mx-1Cre* splenocytes to control levels. Similar results were obtained from BM-derived cultures (*SI Appendix*, Fig. S6*B*). RT-qPCR analysis also showed that *Pparγ* overexpression rescued the induction of the osteoclast transcriptional factor *c-Fos* in PTIP-deficient cells (Fig. 4*E*). These data show that PTIP promotes osteoclast differentiation by transcriptional regulation of *Pparγ*.

To further elucidate the impact of PTIP deletion on the transcriptional regulation of osteoclast differentiation, we isolated osteoclast progenitors (defined as B220/CD3^{-}, Mac-1^{-}, and CD115^{+} cells) (42) from fresh BM of WT *Mx-1Cre* and *Ptip*$^{flox/flox}$ *Mx-1Cre* mice (Fig. 5*A*) and performed genome-wide RNA profiling by RNA sequencing (RNA-seq). Our genome-wide analysis showed that PTIP deletion resulted in the down-regulation of 724 genes and in the up-regulation of 290 genes [false-discovery rate (FDR) ≤0.05, fold change ≥2] (Fig. 5*B*). Along with *Ptip* and *Pparγ*, several osteoclast-related genes were down-regulated in *Ptip*$^{flox/flox}$ *Mx-1Cre* osteoclast progenitors (Fig. 5*B*). Gene set enrichment analysis (GSEA) of RNA-seq data also showed a significant down-regulation of both PPAR signaling pathway-associated genes (Fig. 5*C*) and osteoclast differentiation-associated genes (Fig. 5*D*) upon PTIP deletion in osteoclast progenitors. Furthermore, despite the down-regulation of osteoclast-associated genes, PTIP deletion did not cause changes in the expression levels of the upstream osteoclastogenic RANK and M-CSF receptors in osteoclast progenitors (*SI Appendix*, Fig. S7). Together, these data further illustrate that PTIP deletion leads to intrinsic defects in osteoclast differentiation by transcriptional regulation of *Pparγ* and its downstream targets.

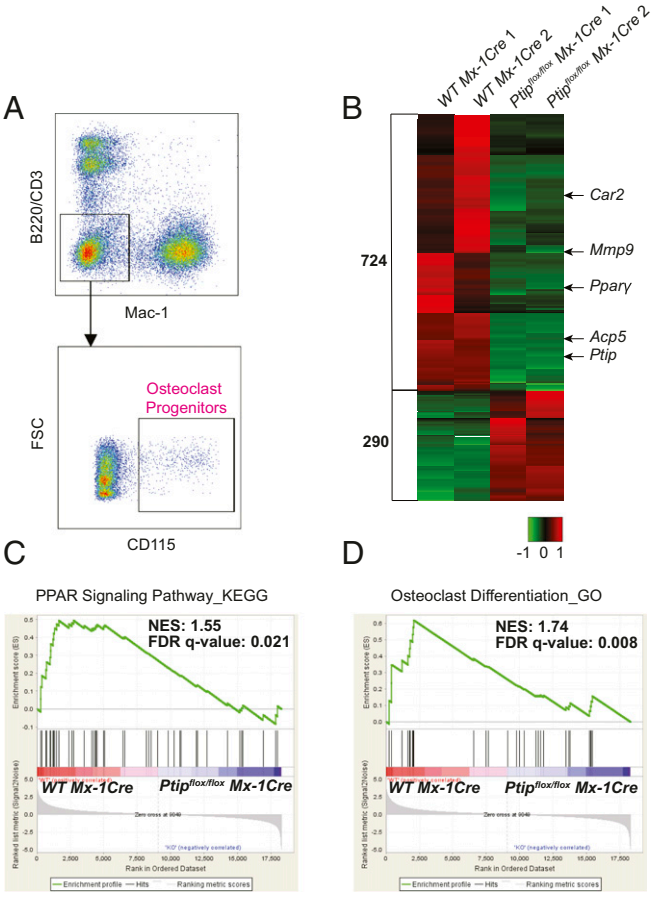

Fig. 5. PTIP deletion leads to down-regulation of an osteoclast-differentiation transcriptional program in osteoclast progenitors. (*A*) Flow cytometry illustrating the sorting scheme for freshly isolated osteoclast progenitors from mouse BM used for RNA-seq analysis. FSC, forward scatter. (*B*) Heat map of genome-wide transcriptome changes in osteoclast progenitor cells isolated from WT *Mx-1Cre* and *Ptip*$^{flox/flox}$ *Mx-1Cre* BM (FDR ≤0.05); arrows highlight *Ptip*, *Pparγ*, *Acp5* (TRAP), *Car2* (carbonic anhydrase-2), and *Mmp9* (matrix metallopeptidase-9) (n = 2). The scale bar denotes the expression level as $\log_2$ value. (*C* and *D*) GSEA plots evaluating changes in the PPAR signaling pathway (*C*) and osteoclast differentiation gene signatures (*D*) upon PTIP deletion (n = 2). Gene sets were obtained from the Broad Institute-based Molecular Signature Database (MSigDB) (68). NES, normalized enrichment score.

PTIP Directly Localizes to the *Pparγ* Promoter and Is Required for the Enrichment of H3K4me and RNA Polymerase II. H3K4me associates with gene activation (43), and endogenous PTIP was shown to be a component of a histone methyltransferase complex that contains the histone H3K4 methyltransferases MLL3 and MLL4 (Kmt2D) (24, 25, 33). In addition, the deletion of PTIP was shown to impair the enrichment of H3K4me3 and RNA polymerase II (Pol II) on the *Pparγ* promoter during adipogenesis (40). To investigate how PTIP regulates *Pparγ* during osteoclastogenesis, we evaluated in vivo interactions taking place in *Pparγ* regulatory regions. We employed ChIP followed by qPCR (ChIP-qPCR) to demonstrate the location of PTIP and its associated active mark H3K4me3 in RANKL-treated spleen- and BM-derived osteoclast precursors. We detected significant enrichment of PTIP in the *Pparγ* promoter region (Fig. 6 *A* and *B*), as well as its associated mark H3K4me3 (Fig. 6 *C* and *D*). PTIP deletion reduced the enrichment of PTIP (Fig. 6 *A* and *B*) as well as H3K4me3 signal (Fig. 6 *C* and *D*). In addition, PTIP deletion also decreased the enrichment of Pol II at the *Pparγ* promoter region (Fig. 6 *E* and *F*). Thus, we conclude that PTIP directly regulates *Pparγ* expression during osteoclastogenesis by binding directly to the *Pparγ* promoter and promoting H3K4me3 and Pol II recruitment.

PTIP Deletion Perturbs the Leukemic Stem Cell Niche in *MLL*-Rearranged AML. Like their normal HSC counterparts, LICs in AML reside in specific niches in the BM (44) and are thought to be the cause for relapse following chemotherapy, thus making targeting of the LIC niche an attractive strategy in AML treatment (45). A study using mouse models of chronic myeloid leukemia (CML) and *MLL*-rearranged AML showed that constitutive parathyroid hormone receptor activation, which increases bone remodeling, differentially attenuated CML progression but stimulated *MLL*-rearranged AML progression (46), suggesting a larger BM niche for *MLL*-rearranged LICs. Since PTIP deletion resulted in decreased medullary space (Fig. 2), we investigated how these changes in the niche affect leukemogenesis in *MLL*-rearranged AML. For this, we used a murine AML model driven by the MLL-AF9 oncogene (47, 48). Murine WT HSPCs were transduced with retrovirus encoding both MLL-AF9 and GFP and were transplanted into irradiated WT *Mx-1Cre* and *Ptip*$^{flox/flox}$ *Mx-1Cre* mice (Fig. 7*A*). Both groups developed AML at the same time (Fig. 7*B*). In this model, LICs have been immunophenotypically defined as Lin^{low} Sca-1^{-} c-Kit^{+} CD16/32^{+} CD34^{+} cells, which share the same immunophenotype as granulocyte-macrophage progenitors (GMPs) and thus are termed "GMP-like leukemia cells" (L-GMPs) (47). Flow cytometry analysis revealed that the LIC/L-GMP fraction was

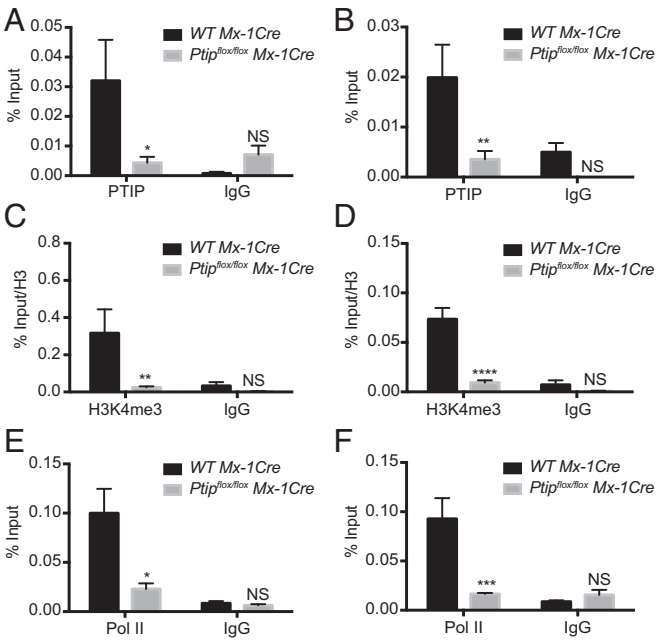

Fig. 6. PTIP directly localizes and promotes chromatin changes at the *Pparγ* promoter. qPCR analysis of ChIP using antibodies against PTIP (*A* and *B*), H3K4me3 (*C* and *D*), and Pol II (*E* and *F*) at the *Pparγ* promoter region in mature osteoclasts differentiated from splenocytes (*Left*) and from BM cells (*Right*) of WT *Mx-1Cre* and *Ptip*$^{flox/flox}$ *Mx-1Cre* mice injected with poly(I:C) ($n = 3$). Bar graphs show mean ± SEM. *$P < 0.05$; **$P < 0.01$; ***$P < 0.005$; ****$P < 0.0001$; NS, not significant ($P > 0.05$).

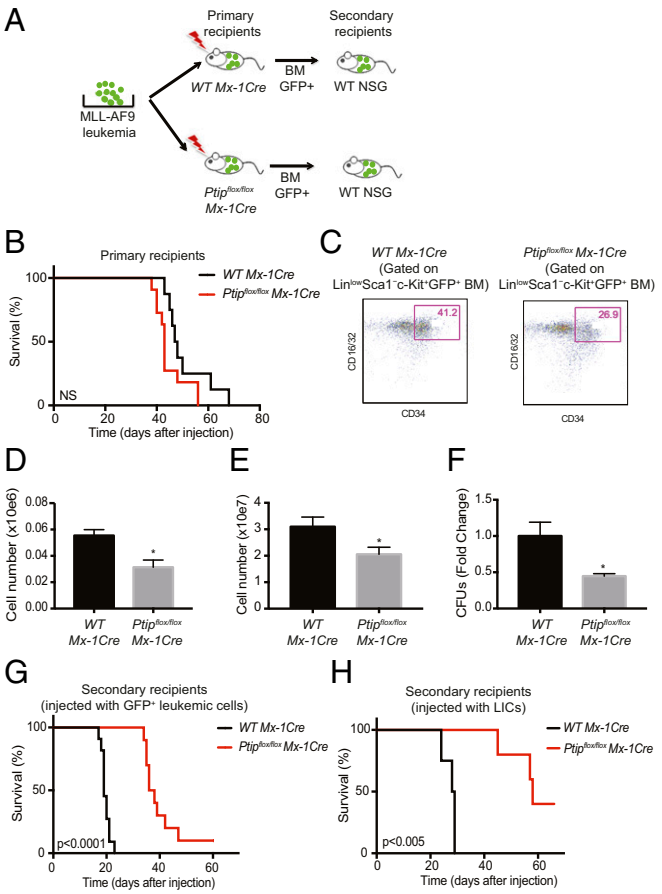

Fig. 7. PTIP deletion perturbs the leukemic stem cell niche. (*A*) Transplantation scheme: BM cells isolated from WT adult mice were infected with retrovirus expressing the *MLL-AF9* fusion gene and GFP as a mark and were injected into sublethally irradiated (550 rad) WT *Mx-1Cre* and *Ptip*$^{flox/flox}$ *Mx-1Cre* primary recipients previously injected with poly(I:C). BM cells isolated from these moribund leukemic primary recipients were sorted by FACS and were injected into NSG secondary recipients. (*B*) The survival curve of the primary transplanted mice ($n = 8$–11; $P > 0.05$, not significant). (*C*) Flow cytometry showing the percentage of LICs, defined as Lin^{low} Sca-1^{-} c-Kit^{+} CD16/32^{+} CD34^{+} cells, in the BM of leukemic primary recipients. One representative of at least three animals is shown. (*D*) The number of LICs in *MLL-AF9*–transformed GFP^{+} BM cells of leukemic primary recipients ($n = 3$). (*E*) Total AML cell numbers in the BM of leukemic primary recipients ($n = 3$). (*F*) BM cells from leukemic primary recipients were plated in methylcellulose medium supplemented with 20% DMEM, 5 ng/mL IL-3, 5 ng/mL IL-6, and 100 ng/mL SCF. Colonies were scored after 10 d of culture ($n = 5$). (*G*) Survival curve of secondary transplanted NSG recipients ($n = 10$–11; $P < 0.0001$). (*H*) Survival curve of NSG mice transplanted with BM LICs from leukemic primary recipients ($n = 4$–5; $P < 0.005$). Bar graphs show mean ± SEM. *$P < 0.05$; NS, not significant ($P > 0.05$).

significantly reduced in the BM of transplanted *Ptip*$^{flox/flox}$ *Mx-1Cre* mice (Fig. 7 *C* and *D*), as was the total number of AML cells in the BM (Fig. 7*E*). Moreover, the BM cells of these mice yielded lower cfu activity than the BM cells of WT *Mx-1Cre* mice in semisolid cultures (Fig. 7*F*). We also found that the number of LICs/L-GMPs was significantly increased while the total AML cell numbers remain similar in the spleen of transplanted *Ptip*$^{flox/flox}$ *Mx-1Cre* mice (*SI Appendix*, Fig. S8). To examine how exposure to a PTIP-deficient BM niche impacts LICs in vivo in this AML model, we performed secondary transplantation of BM AML cells (purified as GFP^{+} live BM cells) isolated from primary recipient WT *Mx-1Cre* and *Ptip*$^{flox/flox}$ *Mx-1Cre* mice into secondary immunocompromised NOD-SCID-γ (NOD.Cg-Prkdc,scid,Il2rg, tm1Wjl/SzJ; NSG) recipients (Fig. 7*A*). All the mice that received AML cells exposed to a WT BM microenvironment succumbed to AML within 25 d posttransplantation (Fig. 7*G*). In contrast, recipients of AML cells exposed to a PTIP-deficient BM microenvironment had significantly extended survival (Fig. 7*G*), suggesting that the LIC fraction is negatively affected by a PTIP-deficient BM microenvironment. We further transplanted BM LICs isolated from primary recipient WT *Mx-1Cre* and *Ptip*$^{flox/flox}$ *Mx-1Cre* mice into NSG recipients. Animals receiving LICs exposed to a WT BM microenvironment developed AML within 30 d of transplantation (Fig. 7*H*), whereas those receiving LICs exposed to a PTIP-deficient BM microenvironment had a significantly longer survival (Fig. 7*H*), suggesting that a PTIP-deficient BM microenvironment also affects the leukemogenic potential of LICs. Taken together, these results indicate that PTIP deletion promotes changes in the BM niche that lead to both a reduced number of LICs in the BM and a reduced leukemogenic potential of the remaining BM LICs.

Discussion

Knowledge of the cellular and molecular determinants of the BM niche has improved markedly in the past few years (3, 49). However, little is known about epigenetic factors that maintain transcriptional programs required for the integrity of the niche. PTIP is a protein associated with transcription that stably associates with a subset of MLL-like complexes containing the MLL3 and MLL4 methyltransferases (23–25). Interestingly, PTIP has also been shown to play a role in the repair of DNA breaks (26, 27). In the hematopoietic compartment, we have previously shown that PTIP promotes chromatin changes critical for Ig class-switch recombination in B cells (29) and controls thymocyte development and immigration (30). However, a role for PTIP in sustaining BM hematopoiesis was, to our knowledge, not investigated.

Here we find that the deletion of PTIP in HSCs and HSPCs disrupts the microenvironment in the BM by blocking osteoclast

differentiation, leading to a reduction of the BM HSPC pool and extramedullary hematopoiesis. At the molecular level, we show that PTIP binds directly to the *Pparγ* promoter and promotes chromatin modifications required for its transcription, which was previously shown to be essential for osteoclastogenesis (32). Indeed, PTIP deficiency closely resembles the phenotype of mice with deletion of *Pparγ* in the hematopoietic lineage: increased bone mass, reduced medullary cavity space, and extramedullary hematopoiesis (32). In both mouse models, this phenotype is the result of a reduced number of osteoclasts without affecting osteoblasts.

Osteoclasts derive from the monocyte lineage, are the only cells definitively shown to degrade bone, and therefore are essential to maintain skeletal integrity (9). Providing a niche for hematopoiesis is a major skeletal function. Indeed, osteoclasts have been shown to regulate HSC functions through their effects on bone remodeling, by modulating local calcium concentrations, by releasing factors from the bone matrix, and by producing cytokines (6–8). In addition to their roles in hematopoiesis, osteoclasts are also key mediators of skeletal diseases. Defects in osteoclast bone resorption cause osteopetrosis, a disease associated with an increased skeletal mass and abnormally dense bone (50). Past studies have implicated epigenetic alterations as key factors of both normal bone-tissue development and function and diseases of pathologic bone remodeling (51). Several studies suggested that DNA methylation plays an important role in osteoblast differentiation (52–54) and in the cross-talk between osteoblasts and osteoclasts (55). Recently, DNA methylation by DNMT3A was shown to regulate osteoclastogenesis by epigenetic repression of IFN regulatory factor 8 (IRF8) (56). The role of histone acetylation and the effects of histone deacetylase inhibitors (HDACi) have also been investigated in bone cells in relation to bone remodeling in conditions characterized by pathological bone loss, including periodontitis, rheumatoid arthritis, and myeloma bone disease (57). Our work showing a role for PTIP in promoting chromatin changes important for maintaining an osteoclast transcriptional program identifies PTIP as an epigenetic factor in osteoclastogenesis, uncovering a previously unrecognized regulator of bone homeostasis.

The importance of identifying and characterizing factors that regulate the HSC niche is underscored by its involvement in myeloid neoplasms (12). It is critical to determine how LICs and their progeny perceive the BM microenvironment to understand how leukemic hematopoiesis can manipulate the niche at the expense of normal hematopoiesis. Here we find that the requirement of PTIP for the integrity of the BM niche is also important to maintain the LIC niche in a mouse model of MLL-AF9 AML. Exposure of MLL-AF9 AML to a PTIP-deficient BM microenvironment led to a reduction in LICs and increased survival upon transplantation (Fig. 7). Reduced trabecular bone mass in retinoic acid receptor γ- or retinoblastoma protein-deficient mice correlates with aggravated myeloproliferative neoplasms (MPNs), suggesting that endosteal niche alterations can promote MPN progression (13, 15). In addition, AML has been associated with increased bone remodeling and the accumulation of osteoblast-primed BM mesenchymal stromal cells, which do not seem to be able to mature into osteoblasts, correlating with decreased mineralized bone (58). In line with our findings, a study using mouse models of CML and MLL-AF9 AML showed that constitutive parathyroid hormone receptor activation, which increases bone remodeling, attenuated CML progression but stimulated MLL-AF9 AML progression (46), suggesting a larger BM niche for MLL-AF9 LICs. The study we report here directly shows that a defect in osteoclastogenesis that leads to reduced bone remodeling and reduced medullary space negatively impacts LICs and slows disease progression in a mouse model of MLL-rearranged AML.

Materials and Methods

Mice. PTIP conditional-knockout mice were generated by crossing *Ptip*$^{flox/flox}$ mice (described in ref. 59) with *Mx1-Cre* mice, in which exon 1 of PTIP is floxed by Cre recombination. All experiments were performed with WT *Mx-1Cre* and *Ptip*$^{flox/flox}$ *Mx-1Cre* mice groups. The WT *Mx-1Cre* group represents mice with *Ptip*$^{flox/flox}$ *Mx-1Cre*$^{-/-}$ or *Ptip*$^{+/+}$ *Mx-1Cre*$^{+/+}$ genotypes, and the *Ptip*$^{flox/flox}$ *Mx-1Cre* mice group represents mice of the *Ptip*$^{flox/flox}$ *Mx-1Cre*$^{+/+}$ genotype. Mice between 8 and 12 wk of age were injected i.p. with 300 μg of poly(I:C) (Sigma Aldrich), five times, every other day. Experiments were performed 3 wk after the last poly(I:C) injection.

NSG mice from Jackson Laboratory were used for secondary BM transplantation.

All animal experiments were approved by the Institutional Animal Care and Use Committee of the University of Texas MD Anderson Cancer Center.

BM Transplantation Assay. For long-term BM reconstitution transplantation, whole BM (WBM) cells were harvested from 6- to 10-wk-old *PTIP*$^{flox/flox}$ *Mx-1Cre* mice (CD45.2), and T lymphocytes were depleted with CD90.2 magnetic beads (Miltenyi). The BM hematopoietic cell fraction without T lymphocytes (3×10^6 to 6×10^6) was injected i.v. into lethally irradiated (950 rad) recipients (CD45.1). Five weeks after transplantation, recipient mice were divided into two groups. One group was treated with poly(I:C) as described previously; the other group was kept as control. Beginning 5 wk after the last dose of poly(I:C) and continuing for 11 wk, blood was obtained from the cheek of recipient mice, subjected to hemolysis of RBCs (ACK lysing buffer; Quality Biological), and stained with antibodies to monitor engraftment. For mixed BM transplantation, WBM cells were harvested from poly(I:C)-treated *Ptip*$^{flox/flox}$ *Mx-1Cre* mice (CD45.2), and T lymphocytes were depleted with CD90.2 magnetic beads (Miltenyi). The BM hematopoietic cell fraction without T lymphocytes was mixed in a 1:1 ratio with WT WBM (CD45.1) and transplanted into lethally irradiated (950 rad) WT *Mx-1Cre* and *Ptip*$^{flox/flox}$ *Mx-1Cre* recipients (CD45.2). Beginning 5 wk after transplantation and continuing for 11 wk, reconstitution levels were monitored in the peripheral blood as described above.

Tissue Processing, Cell Isolation, and Flow Cytometry. On the day of the experiment, blood was collected to perform complete blood counts and WBC differential analysis by using the HEMAVET HV950FS instrument (Drew Scientific Inc.). After mice were killed, body and spleen weights were determined. Spleens were fixed in formalin and then were embedded in paraffin blocks for histological staining. Long bones were dissected and processed for immunohistology and/or μCT, as described in the following sections.

Spleen cell suspensions were prepared by gently grinding the organs through 40-μm cell strainers with ice-cold PBS (Corning Cellgro). BM cells were flushed out from the long bones (tibias and femurs). Isolated spleen and BM cells were stained with acridine orange/propidium iodide and counted using the Nexcelom Cellometer.

For flow cytometry analysis and cell sorting, cells were stained in PBS supplemented with 2% heat-inactivated FBS (Gemini Bio-Products). The following antibodies were used: B220 PE, CD11b (Mac-1) PE or AF647, CD11c PE, CD4 PE, CD8 PE, NK1.1 PE, Ter119 PE, CD3 PE, c-Kit APC or PerCP-cy5, CD34 AF647, Ly6G/6C (Gr-1) APC, CD45.1 FITC, CD45.2 biotin (BD Biosciences), Sca-1 PEcy7, CD11b (Mac-1) biotin (eBioscience), CD254 (RANKL) PE, CD16/CD32 BV421, CD115 (M-CSF receptor) PEcy7 (BioLegend), and streptavidin PacBlue (Thermo Fisher Scientific). DAPI or Zombie Aqua (BioLegend) was used to exclude dead cells. Flow cytometry was performed on a Gallios or Gallios 561 instrument (Beckman Coulter). Osteoclast progenitor and leukemic cell-sorting secondary transplantation were performed on a BD FACS Aria II cell sorter (BD Biosciences). LIC sorting was performed on a MoFlo Astrios instrument (Beckman Coulter).

Immunohistochemistry. Mice femurs were fixed in buffered formalin for 24 h, decalcified for 8 d, and embedded in paraffin blocks for sectioning at a thickness of 10 μm. The sections were deparaffinized with xylene and hydrated before immunohistochemical staining. Subsequently, endogenous peroxidase activity was blocked with 3% H_2O_2 for 10 min in the dark. For antigen retrieval, a citrate buffer (10 mM, pH 5.0) and a microwave (400 W, 3 min at full power and 10 min at half power) were used. Slides were cooled, and nonspecific antibody binding was prevented by incubating slides with Background Sniper (Biocare Medical). Slides were then incubated with the primary antibody for 30 min at room temperature. TRAP antibody (Abcam) was used for osteoclast detection, and ALP antibody (Santa Cruz Biotechnology, Inc.) was used for osteoblast detection. Immunoreactivity was

detected using EnVision+ System HRP-Labeled Polymer Anti-rabbit (Dako), followed by incubation with the Liquid DAB+ Substrate Chromogen System (Dako). Slides were counterstained with hematoxylin, dehydrated, and mounted with Cytoseal 60 (Thermo Fisher Scientific). Negative controls were obtained by replacing the primary antibodies with antibody diluents, yielding no signals. Whole-slide images were scanned and processed using an Aperio ScansScope CS system (Leica Biosystems) with a 20× objective. Three to five areas per slide were randomly selected with Spectrum ImageScore v10.2.2 (Leica Biosystems). The number of $TRAP^+$ or ALP^+ cells in each field of view were counted. TRAP staining was also performed by enzymatic reactions after the bones were processed with plastic sectioning. The reagents used for enzymatic reactions include sodium tartrate dibasic dehydrate, naphthol AS-MX phosphate, and Fast Red TR Salt hemi(zinc chloride) salt (all from Sigma-Aldrich).

Biochemical Marker Study for Bone Resorption and Bone Formation. As a bone resorption marker, urine deoxypyridinoline cross-links were measured with the MicroVue DPD EIA kit (Quidel) and were normalized by urinary creatinine level measured with the MicroVue Creatinine EIA kit (Quidel). As bone-formation markers, serum alkaline phosphatase was measured with the QuantiChrom Alkaline Phosphatase assay kit (BioAssay Systems), and serum osteocalcin was measured with the Mouse Osteocalcin Enzyme Immunoassay kit (Alfa Aesar).

μCT of Trabecular Bones. Trabecular bone morphometry within the metaphyseal region of the distal femur was quantified by μCT (ScanXmate-RX; Comscantechno Co., Ltd.). 3D microstructural image data were reconstructed, and bone morphometric analysis was performed using TRI/3D-BON software (RATOC System Engineering Co., Ltd.).

In Vitro Osteoclast Differentiation and TRAP Staining. The osteoclast differentiation assay from isolated splenocytes or BM cells was modified from refs. 60 and 61. Isolated BM and spleen cells were passed through 40-μm cell strainers and cultured overnight in alpha-MEM medium (Gibco) containing 10% heat-inactivated FBS (Gemini Bio-Products), 100 U/mL penicillin, and 100 mg/mL streptomycin (Corning). On the next day, nonadherent cells were harvested and seeded with equal densities into 35-mm plates (Corning) in alpha-MEM medium with 50 ng/mL of M-CSF (Gibco), 10% heat-inactivated FBS, 100 U/mL penicillin, and 100 mg/mL streptomycin. After 3 d of culture in M-CSF, the medium was removed along with nonadherent cells, and fresh osteoclast medium [alpha-MEM medium supplemented with M-CSF (50 ng/mL), RANKL (50 ng/mL) (R&D systems), 10% heat-inactivated FBS, 100 U/mL penicillin, and 100 mg/mL streptomycin] was added. During the next 3 d of culture, cells were washed with PBS, and osteoclast medium was replaced daily.

After 6 d of osteoclast differentiation, cultured adherent cells were stained for TRAP or were harvested for total RNA isolation/ChIP. For TRAP staining, cells were fixed with 4% paraformaldehyde (Thermo Fisher Scientific) in PBS for 1 h at 4 °C and were stained with the Leukocyte Acid Phosphatase (TRAP+) Kit (Sigma Aldrich) according to the manufacturer's protocols. Mature osteoclasts were identified as multinucleated (more than four nuclei) $TRAP^+$ cells and were counted using an Olympus 1×83 microscope.

Plasmids, PPARγ Overexpression, and Generation of Leukemia in Vivo. The MSCV-MLL-AF9-IRES-GFP plasmid was a gift from S. Armstrong, Dana-Farber Cancer Institute, Harvard Medical School, Boston. MSCV-Empty-puromycin and MSCV-PPARγ-puromycin plasmids were provided by K.G. To overexpress PPARγ in splenocytes and BM cells, BOSC23 cells were transfected with MSCV-Empty-puromycin or MSCV-PPARγ-puromycin and pCL-Eco helper plasmid using XtremeGene9 DNA transfection reagent (Roche). After 48 h, the viral supernatant was transferred to splenocytes and BM cells with 4 μg/mL Polybrene in alpha-MEM (Gibco-Invitrogen) supplemented with 10% heat-inactivated FBS, 100 U/mL penicillin, and 100 mg/mL streptomycin. After infection, cells were subjected to in vitro osteoclast differentiation as described above for 36 h before being selected with 0.5 μg/mL puromycin. After 6 d of culture, mature osteoclasts (with more than four nuclei) were identified and were counted under a microscope. Cells were harvested, and total RNA was isolated for gene expression. To generate MLL-AF9–infected cells, retrovirus was used to infect BM cells harvested 4 d after administration of 5-fluorouracil (250 mg/kg). BOSC23 cells were transfected with MSCV-MLL-AF9-IRES-GFP and pCL-Eco helper plasmid using XtremeGene9 DNA transfection reagent (Roche). After 48 h and 72 h of transfection, the viral supernatant was transferred onto BM cells with 5 ng/mL IL-3, 5 ng/mL IL-6, 100 ng/mL stem cell factor (SCF), and 4 μg/mL Polybrene (all from PeproTech) in DMEM (Gibco) supplemented with 10% heat-inactivated FBS, 100 U/mL penicillin, and 100 mg/mL streptomycin. After infection, cells were maintained in methylcellulose (M3432; STEMCELL Technologies) supplemented with 20% DMEM, 5 ng/mL IL-3, 5 ng/mL IL-6, and 100 ng/mL SCF. Five days after infection, 1×10^5 GFP^+ cells were injected i.v. into sublethally irradiated WT *Mx-1Cre* and *Ptip*$^{flox/flox}$ *Mx-1Cre* recipients (550 rad) to generate leukemia in vivo. For secondary transplantation, 1×10^5 GFP^+ cells or 10,000 LICs from primary recipient mice were sorted and transplanted into NSG mice. We use immunocompromised (NSG) strains as secondary transplantation hosts to avoid irradiation. WBC counts were performed with a HEMAVET HV950FS instrument to confirm leukemia in the recipients.

Colony-Forming Assay. For colony-forming assays, 5,000 BM cells from primary recipient mice were plated in methylcellulose (M3234; STEMCELL Technologies) supplemented with 20% DMEM, 5 ng/mL IL-3, 5 ng/mL IL-6, and 100 ng/mL SCF, according to the manufacturer's instructions. The number of colonies was determined after 10 d in culture.

Gene-Expression Analysis, Western Blot, and ChIP.

RT-qPCR. Cells were spun down and washed once with cold PBS; then RNA was isolated with a Qiagen RNeasy kit (Qiagen) according to the manufacturer's protocol. One microgram of total RNA was treated with amplification-grade DNaseI (Qiagen) and was reverse-transcribed with the SuperScript III SuperMix system (Invitrogen), according to the manufacturers' protocols. mRNA levels were analyzed via RT-qPCR analysis using the iTaq SYBR Green Supermix (Bio-Rad Laboratories), according to the manufacturer's protocol. Reactions were performed on an ABI 7900HT Fast Real-Time PCR system or a 7500 Fast Real-Time PCR System (Thermo Fisher Scientific). Samples were normalized to transcripts encoding *Gapdh*. Primers for RT-qPCR reactions are listed in *SI Appendix*, Table S1.

Western blot analysis. $CD45^+$ BM cells were sorted by magnetically activated cell sorting (Miltenyi Biotech). Cells were lysed in radioimmunoprecipitation (RIPA) buffer with Halt protease inhibitor mixture (Thermo Fisher Scientific), sonicated on ice, and spun at 14,000 × *g* for 15 min at 4 °C. The supernatant was assayed for protein concentration with a Pierce BCA protein assay kit (Thermo Fisher Scientific). Protein was resolved by 10% Tris·HCl polyacrylamide gel (Bio-Rad Laboratories) and was transferred to PVDF membranes for blotting. Blots were blocked with 5% milk in Tris-buffered saline with 0.1% Tween 20 (Sigma Aldrich) at room temperature and then were incubated with primary antibodies [1:1,000 anti-PTIP (provided by K.G.); 1:1,000 anti-Pparγ (Santa Cruz); 1:10,000 anti–β-actin (Abcam) in blocking buffer] at 4 °C overnight. Blots were then incubated with secondary antibody at room temperature for 1 h. Blots were developed with Amersham ECL Western Blotting Detection Reagents (GE Healthcare) or Western Lightning Plus-ECL (Perkin-Elmer, Inc.).

ChIP analysis. After cells were assayed for osteoclast formation, they were washed twice in warm PBS, trypsinized, and resuspended in warm medium containing 0.1 volume cross-linking solution (62). ChIP reactions were performed as described previously (63), followed by DNA purification with a QIAquick PCR Cleanup Kit (Qiagen). Antibodies used include anti-PTIP (provided by K.G.), anti-H3K4me3 (Millipore), and anti-Pol II (Millipore). Antibodies for modified histones, Pol II, and PTIP were added at 1–5 μg per ChIP reaction. The concentration of IgG (Millipore) was adjusted from 1 μg to 5 μg as appropriate. For RT-qPCR analysis, real-time PCR was performed with the iTaq SYBR Green Supermix (Bio-Rad Laboratories) according to the manufacturer's protocol. Primer sequences were derived from the proximal promoter region of *Pparγ*, *Gapdh*, and an untranscribed region on chromosome 6 (UNTR6) (*SI Appendix*, Table S1). Reactions were performed on an ABI 7900HT Fast Real-Time PCR system. Primers used in this study are listed in *SI Appendix*, Table S1.

RNA-Seq. RNA-seq libraries were made from total RNA isolated from osteoclast progenitors sorted from WT *Mx-1Cre* or *Ptip*$^{flox/flox}$ *Mx-1Cre* BM using the Illumina TruSeq Stranded mRNA kit according to the manufacturer's protocol. The libraries were sequenced using the 2 × 75 bases paired-end protocol on an Illumina HiSeq 3000 instrument. A total of four libraries (two biological replicates per condition) were sequenced in one lane, generating 92–103 million pairs of reads per sample. Each pair of reads represents a cDNA fragment from the library.

Mapping. The reads were mapped to the mouse genome (mm10) by TopHat (version 2.0.10) (64). By reads, the overall mapping rate is ∼97%. Approximately 96% of fragments have both ends mapped to the mouse genome.

Differential expression. The number of fragments in each known gene from GENCODE Release M17 (65) was enumerated using htseq-count from the HTSeq package (version 0.6.0) (66). Genes with fewer than 10 fragments in all samples were removed before differential expression analysis. The

differential expression between conditions was statistically assessed by the R/Bioconductor package edgeR (version 3.8.6) (67). Genes FDR ≤0.05, fold change ≥2, and length >200 bp were called as differentially expressed.

Landscape profile of RNA-seq signal. For the fragments that had both ends mapped, the first reads were kept. Together with the reads from the fragments that had only one end mapped, every read was extended to its 3′ end by 200 bp in exon regions. For each read, a weight of 1/*n* was assigned, where *n* is the number of positions to which the read was mapped. The sum of weights for all the reads that cover each genomic position was rescaled to normalize the total number of fragments to 1 M and was averaged over 10-bp resolution. The normalized values were displayed using the University of California, Santa Cruz genome browser (genome.ucsc.edu/).

Gene clustering and heatmap. Hierarchical clustering was performed by the hclust function in R using gene-expression values estimated by edgeR. Before clustering, the expression values of each gene across samples were centered by median and were rescaled so that the sum of the squares of the values is 1.0. Euclidean distance and the ward.D2 clustering method were used for the clustering of the genes. The heatmap was plotted by heatmap.2 function in R.

GSEA. Gene sets were chosen from the GSEA Molecular Signature Database (MSigDB) (software.broadinstitute.org/gsea/msigdb). GSEA was performed by GSEA software (version 3.0) (68). The expression values estimated by edgeR for all the genes were taken as the expression dataset. The permutation type was set as "gene_set," and all of the other parameters were set as default.

Statistical Analysis. Multiple independent biological experiments were performed to assess the reproducibility of experimental findings. Each group is presented by mean ± SEM. To compare two experimental groups, statistical tests were conducted using R statistical language (www.r-project.org/). Unpaired, two-tailed *t* tests were used for all analyses. For ex vivo experiments, multiple independent biological replicates were used. For leukemia transplantation, animals were placed in different experimental groups, and disease development was assessed blindly without prior knowledge of genotype. The significance between the longevity of cohorts was assessed by Kaplan–Meier survival analysis and log-rank (Mantel–Cox) tests. *P* values <0.05 were considered significant to reject the null hypothesis. No randomization was used in any experiment. For statistical analysis of RT-qPCR and ChIP-qPCR data, for analysis of gene expression, the measured cycle threshold (CT) experimental values for each transcript were compiled and normalized to the reference gene *Gapdh* (NM_008084). Normalized expression levels were calculated using the ΔΔCT method described previously (69). Values from these calculations were transferred into the statistical analysis program GraphPad (GraphPad Software Inc.), and unpaired, two-tailed *t* tests were run to assay differences between control and treated cells. For quantitative analysis of candidate gene-regulatory region enrichment, ChIP samples were normalized to 10% input, and data were analyzed using the formula previously described (70). The cumulative mean from each of the three independent experiments was calculated, and the SEM was derived. The statistical analysis package GraphPad was used to measure statistical significance using unpaired, two-tailed *t* tests.

ACKNOWLEDGMENTS. We thank all members of the M.A.S. laboratory, M. Bedford, and C. Y. King for discussions and M. Weiss and S. Stratton for technical help. Core facilities were supported by NIH Grant CA 16672 and Cancer Prevention Research Institute of Texas Grants RP120348, RP170002, and RP170628. This work was supported by Cancer Prevention Research Institute of Texas Recruitment of First-time Tenure-Track Faculty Award RR150039, Sidney Kimmel Foundation-Kimmel Scholar Award SKF-16-061, a National Cancer Institute Cancer Center Support Grant New Faculty Award, an Andrew Sabin Family Fellow Award, and an American Society of Hematology Junior Faculty Scholar Award (to M.A.S.).

1. Orkin SH, Zon LI (2008) Hematopoiesis: An evolving paradigm for stem cell biology. *Cell* 132:631–644.
2. Lord BI, Testa NG, Hendry JH (1975) The relative spatial distributions of CFUs and CFUc in the normal mouse femur. *Blood* 46:65–72.
3. Crane GM, Jeffery E, Morrison SJ (2017) Adult haematopoietic stem cell niches. *Nat Rev Immunol* 17:573–590.
4. Kusumbe AP, Ramasamy SK, Adams RH (2014) Coupling of angiogenesis and osteogenesis by a specific vessel subtype in bone. *Nature* 507:323–328.
5. Kusumbe AP, et al. (2016) Age-dependent modulation of vascular niches for haematopoietic stem cells. *Nature* 532:380–384.
6. Adams GB, et al. (2006) Stem cell engraftment at the endosteal niche is specified by the calcium-sensing receptor. *Nature* 439:599–603.
7. Kollet O, et al. (2006) Osteoclasts degrade endosteal components and promote mobilization of hematopoietic progenitor cells. *Nat Med* 12:657–664.
8. Mansour A, Wakkach A, Blin-Wakkach C (2012) Role of osteoclasts in the hematopoietic stem cell niche formation. *Cell Cycle* 11:2045–2046.
9. Charles JF, Aliprantis AO (2014) Osteoclasts: More than 'bone eaters'. *Trends Mol Med* 20:449–459.
10. Duarte D, et al. (2017) Inhibition of endosteal vascular niche remodeling rescues hematopoietic stem cell loss in AML. *Cell Stem Cell* 22:64–77.
11. Kim YW, et al. (2008) Defective notch activation in microenvironment leads to myeloproliferative disease. *Blood* 112:4628–4638.
12. Korn C, Méndez-Ferrer S (2017) Myeloid malignancies and the microenvironment. *Blood* 129:811–822.
13. Walkley CR, et al. (2007) A microenvironment-induced myeloproliferative syndrome caused by retinoic acid receptor gamma deficiency. *Cell* 129:1097–1110.
14. Walkley CR, Orkin SH (2006) Rb is dispensable for self-renewal and multilineage differentiation of adult hematopoietic stem cells. *Proc Natl Acad Sci USA* 103:9057–9062.
15. Walkley CR, Shea JM, Sims NA, Purton LE, Orkin SH (2007) Rb regulates interactions between hematopoietic stem cells and their bone marrow microenvironment. *Cell* 129:1081–1095.
16. Nair RR, Tolentino J, Hazlehurst LA (2010) The bone marrow microenvironment as a sanctuary for minimal residual disease in CML. *Biochem Pharmacol* 80:602–612.
17. Krivtsov AV, Armstrong SA (2007) MLL translocations, histone modifications and leukaemia stem-cell development. *Nat Rev Cancer* 7:823–833.
18. Lin C, et al. (2010) AFF4, a component of the ELL/P-TEFb elongation complex and a shared subunit of MLL chimeras, can link transcription elongation to leukemia. *Mol Cell* 37:429–437.
19. Mohan M, et al. (2010) Linking H3K79 trimethylation to Wnt signaling through a novel Dot1-containing complex (DotCom). *Genes Dev* 24:574–589.
20. Yokoyama A, Lin M, Naresh A, Kitabayashi I, Cleary ML (2010) A higher-order complex containing AF4 and ENL family proteins with P-TEFb facilitates oncogenic and physiologic MLL-dependent transcription. *Cancer Cell* 17:198–212.
21. Canela A, et al. (2017) Genome organization drives chromosome fragility. *Cell* 170:507–521.e18.
22. Ruthenburg AJ, Allis CD, Wysocka J (2007) Methylation of lysine 4 on histone H3: Intricacy of writing and reading a single epigenetic mark. *Mol Cell* 25:15–30.
23. Cho YW, et al. (2007) PTIP associates with MLL3- and MLL4-containing histone H3 lysine 4 methyltransferase complex. *J Biol Chem* 282:20395–20406.
24. Issaeva I, et al. (2007) Knockdown of ALR (MLL2) reveals ALR target genes and leads to alterations in cell adhesion and growth. *Mol Cell Biol* 27:1889–1903.
25. Patel SR, Kim D, Levitan I, Dressler GR (2007) The BRCT-domain containing protein PTIP links PAX2 to a histone H3, lysine 4 methyltransferase complex. *Dev Cell* 13:580–592.
26. Muñoz IM, Rouse J (2009) Control of histone methylation and genome stability by PTIP. *EMBO Rep* 10:239–245.
27. Panier S, Boulton SJ (2014) Double-strand break repair: 53BP1 comes into focus. *Nat Rev Mol Cell Biol* 15:7–18.
28. Callen E, et al. (2013) 53BP1 mediates productive and mutagenic DNA repair through distinct phosphoprotein interactions. *Cell* 153:1266–1280.
29. Daniel JA, et al. (2010) PTIP promotes chromatin changes critical for immunoglobulin class switch recombination. *Science* 329:917–923.
30. Callen E, et al. (2012) The DNA damage- and transcription-associated protein paxip1 controls thymocyte development and emigration. *Immunity* 37:971–985.
31. Su D, et al. (2017) PTIP chromatin regulator controls development and activation of B cell subsets to license humoral immunity in mice. *Proc Natl Acad Sci USA* 114:E9328–E9337.
32. Wan Y, Chong LW, Evans RM (2007) PPAR-gamma regulates osteoclastogenesis in mice. *Nat Med* 13:1496–1503.
33. Cho EA, Prindle MJ, Dressler GR (2003) BRCT domain-containing protein PTIP is essential for progression through mitosis. *Mol Cell Biol* 23:1666–1673.
34. Santos MA, et al. (2014) DNA-damage-induced differentiation of leukaemic cells as an anti-cancer barrier. *Nature* 514:107–111.
35. Sims NA, Martin TJ (2014) Coupling the activities of bone formation and resorption: A multitude of signals within the basic multicellular unit. *Bonekey Rep* 3:481.
36. Boyle WJ, Simonet WS, Lacey DL (2003) Osteoclast differentiation and activation. *Nature* 423:337–342.
37. Teitelbaum SL (2000) Bone resorption by osteoclasts. *Science* 289:1504–1508.
38. Karsenty G, Wagner EF (2002) Reaching a genetic and molecular understanding of skeletal development. *Dev Cell* 2:389–406.
39. Wada T, Nakashima T, Hiroshi N, Penninger JM (2006) RANKL-RANK signaling in osteoclastogenesis and bone disease. *Trends Mol Med* 12:17–25.
40. Cho YW, et al. (2009) Histone methylation regulator PTIP is required for PPARgamma and C/EBPalpha expression and adipogenesis. *Cell Metab* 10:27–39.
41. Grigoriadis AE, et al. (1994) c-Fos: A key regulator of osteoclast-macrophage lineage determination and bone remodeling. *Science* 266:443–448.
42. Jacome-Galarza CE, Lee SK, Lorenzo JA, Aguila HL (2013) Identification, characterization, and isolation of a common progenitor for osteoclasts, macrophages, and dendritic cells from murine bone marrow and periphery. *J Bone Miner Res* 28:1203–1213.
43. Li B, Carey M, Workman JL (2007) The role of chromatin during transcription. *Cell* 128:707–719.
44. Ishikawa F, et al. (2007) Chemotherapy-resistant human AML stem cells home to and engraft within the bone-marrow endosteal region. *Nat Biotechnol* 25:1315–1321.

45. Krause DS, Van Etten RA (2007) Right on target: Eradicating leukemic stem cells. *Trends Mol Med* 13:470–481.
46. Krause DS, et al. (2013) Differential regulation of myeloid leukemias by the bone marrow microenvironment. *Nat Med* 19:1513–1517.
47. Krivtsov AV, et al. (2006) Transformation from committed progenitor to leukaemia stem cell initiated by MLL-AF9. *Nature* 442:818–822.
48. Somervaille TC, Cleary ML (2006) Identification and characterization of leukemia stem cells in murine MLL-AF9 acute myeloid leukemia. *Cancer Cell* 10:257–268.
49. Schepers K, Campbell TB, Passegué E (2015) Normal and leukemic stem cell niches: Insights and therapeutic opportunities. *Cell Stem Cell* 16:254–267.
50. Tolar J, Teitelbaum SL, Orchard PJ (2004) Osteopetrosis. *N Engl J Med* 351:2839–2849.
51. Husain A, Jeffries MA (2017) Epigenetics and bone remodeling. *Curr Osteoporos Rep* 15:450–458.
52. Cho YD, et al. (2014) Epigenetic modifications and canonical wingless/int-1 class (WNT) signaling enable trans-differentiation of nonosteogenic cells into osteoblasts. *J Biol Chem* 289:20120–20128.
53. Kang MI, et al. (2007) Transitional CpG methylation between promoters and retroelements of tissue-specific genes during human mesenchymal cell differentiation. *J Cell Biochem* 102:224–239.
54. Zhang RP, Shao JZ, Xiang LX (2011) GADD45A protein plays an essential role in active DNA demethylation during terminal osteogenic differentiation of adipose-derived mesenchymal stem cells. *J Biol Chem* 286:41083–41094.
55. Delgado-Calle J, et al. (2012) Role of DNA methylation in the regulation of the RANKL-OPG system in human bone. *Epigenetics* 7:83–91.
56. Nishikawa K, et al. (2015) DNA methyltransferase 3a regulates osteoclast differentiation by coupling to an S-adenosylmethionine-producing metabolic pathway. *Nat Med* 21:281–287.
57. Cantley MD, Zannettino ACW, Bartold PM, Fairlie DP, Haynes DR (2017) Histone deacetylases (HDAC) in physiological and pathological bone remodelling. *Bone* 95: 162–174.
58. Hanoun M, et al. (2014) Acute myelogenous leukemia-induced sympathetic neuropathy promotes malignancy in an altered hematopoietic stem cell niche. *Cell Stem Cell* 15:365–375.
59. Kim D, Wang M, Cai Q, Brooks H, Dressler GR (2007) Pax transactivation-domain interacting protein is required for urine concentration and osmotolerance in collecting duct epithelia. *J Am Soc Nephrol* 18:1458–1465.
60. Stechschulte LA, et al. (2016) PPARG post-translational modifications regulate bone formation and bone resorption. *EBioMedicine* 10:174–184.
61. Tevlin R, et al. (2014) Osteoclast derivation from mouse bone marrow. *J Vis Exp,* e52056.
62. Kondo Y, Shen L, Yan PS, Huang TH, Issa JP (2004) Chromatin immunoprecipitation microarrays for identification of genes silenced by histone H3 lysine 9 methylation. *Proc Natl Acad Sci USA* 101:7398–7403.
63. Martens JA, Wu PY, Winston F (2005) Regulation of an intergenic transcript controls adjacent gene transcription in Saccharomyces cerevisiae. *Genes Dev* 19:2695–2704.
64. Kim D, et al. (2013) TopHat2: Accurate alignment of transcriptomes in the presence of insertions, deletions and gene fusions. *Genome Biol* 14:R36.
65. Mudge JM, Harrow J (2015) Creating reference gene annotation for the mouse C57BL6/J genome assembly. *Mamm Genome* 26:366–378.
66. Anders S, Pyl PT, Huber W (2015) HTSeq–A Python framework to work with high-throughput sequencing data. *Bioinformatics* 31:166–169.
67. Robinson MD, McCarthy DJ, Smyth GK (2010) edgeR: A Bioconductor package for differential expression analysis of digital gene expression data. *Bioinformatics* 26: 139–140.
68. Subramanian A, et al. (2005) Gene set enrichment analysis: A knowledge-based approach for interpreting genome-wide expression profiles. *Proc Natl Acad Sci USA* 102: 15545–15550.
69. Schmittgen TD, Livak KJ (2008) Analyzing real-time PCR data by the comparative C(T) method. *Nat Protoc* 3:1101–1108.
70. Mukhopadhyay A, Deplancke B, Walhout AJ, Tissenbaum HA (2008) Chromatin immunoprecipitation (ChIP) coupled to detection by quantitative real-time PCR to study transcription factor binding to DNA in Caenorhabditis elegans. *Nat Protoc* 3:698–709.